










Synthesis and Characterization of Methionine-Functionalized Boehmite with Enhanced Removal of Methyl Orange

Ery Susiany Retnoningtyas^{1,2} , Yi-Hsu Ju^{1,3,4} , Suryadi Ismadji^{1,2} , Chintya Gunarto² , Aning Ayucitra² , Alchris Woo Go³ , Shella Permatasari Santoso^{1,2} , Nathania Puspitasari² , Artik Elisa Angkawijaya^{3,*} 

¹ Department of Chemical Engineering, National Taiwan University of Science and Technology, Taipei 106-07, Taiwan;

² Department of Chemical Engineering, Widya Mandala Catholic University Surabaya, Surabaya 601-14, Indonesia;

³ Graduate Institute of Applied Science and Technology, National Taiwan University of Science and Technology, Taipei 106-07, Taiwan;

⁴ Taiwan Building Technology Center, National Taiwan University of Science and Technology, Keelung Road, 10607, Taipei City, Da'an District, Taipei City, Taiwan;

* Correspondence: artikelisa@mail.ntust.edu.tw (A.E.A.);

Scopus Author ID 37027954600

Received: 25.08.2021; Revised: 29.09.2021; Accepted: 2.10.2021; Published: 24.10.2021

Abstract: Methionine, an amino acid with thioether, carboxyl, and amino functional groups, was used to enhance the adsorption capacity of boehmite toward methyl orange (MO). An environmentally friendly synthesis method was performed to prepare the methionine-functionalized boehmite (MFB) at 70°C using water as the solvent. The MFB has prominent XRD characteristic peaks at $2\theta = 14.5^\circ$, 28.6° , 38.4° , and 48.4° . The addition of functional groups from methionine was indicated by the appearance of FTIR bands at 2094, 1424, and 1220 cm^{-1} corresponding to carboxyl, amino, and thioether groups, respectively. The N_2 isotherm curve indicates the mesoporous structure of MFB, with surface area, pore-volume, and mean pore width of $287\text{ m}^2\text{ g}^{-1}$, $0.996\text{ cm}^3\text{ g}^{-1}$, 13.85 nm, respectively. The kinetic adsorption data showed a good fitting with the pseudo-first-order model, where the equilibrium can be achieved within 50 min. The adsorption of MO by MFB was better correlated with the Langmuir model with a maximum adsorption capacity of $167.4075\text{ mg g}^{-1}$, which was achieved at 323 K. The thermodynamic study reveals that the adsorption of MO on MFB was an endothermic and spontaneous process.

Keywords: aluminum; boehmite, methionine; methyl orange; adsorption.

© 2021 by the authors. This article is an open-access article distributed under the terms and conditions of the Creative Commons Attribution (CC BY) license (<https://creativecommons.org/licenses/by/4.0/>).

1. Introduction

The constant population growth and rapid industrial/societal development consequently escalate the use of synthetic dyes in textile, medicinal, food, plastics, and cosmetics manufacturing [1-3]. For these coloring purposes, over 700,000 tons of synthetic dyes were created per year. Up to 15% of these dyes were reportedly leached out due to unsystematic disposal where it ended in the water bodies [4-10]. The dye-contaminated water is postulated to trigger various toxicological and carcinogenic effects on humans and the ecosystems [11-14]. Therefore, appropriate treatment is essential to accommodate the demand for clean water globally [15]. Dye removal through physical processes (such as adsorption) is preferable to the chemical approach, which often involves harmful chemicals. Adsorption is a reliable, simple

physical technique for dye removal attributed to its low cost, low energy requirement, high feasibility, high removal efficiency, high reusability, and minimal by-products [16]. The selection of adsorbent with a high adsorption capability emerges as one of the most crucial factors in guaranteeing the successful removal of hazardous pollutants [6,17,18].

In the past decade, metal oxides were postulated to possess a good adsorption affinity towards many ionic pollutants and had been widely utilized to remove various hazardous substances from the water. Their frequent application as adsorbent was contributed by the low-cost, straightforward synthesis and modifiable properties [19,20]. Boehmite, a dimorphous material containing diascore γ -AlOOH and γ -Al₂O₃, is a class of metal oxide with hydroxide moiety. Boehmite is known to have a sorption ability toward organic and inorganic compounds, besides its potential in other applications such as catalysts [21,22], ceramics [23,24], abrasives [25], and filters [26]. There have been some reports that demonstrated the enhanced adsorption capacity of boehmite by the functionalization technique. The addition of tetraethylenepentamine (TEPA) during the preparation of amino-functionalized boehmite gave a nearly two-fold increase in the adsorption capacity toward Cr [27]. In another study, the boehmite modification through the addition of chitosan reportedly shows up to 3-fold enhanced Cr adsorption compared to the unmodified boehmite [28]. Herein, functionalization of boehmite was conducted by introducing methionine, a compound containing multiple functional groups. Methionine with amino (—NH_2), carboxylic (—COOH), and thioether (R—S—R) functional groups [29,30] can provide additional binding sites to increase the number of active adsorption sites of boehmite.

Synthesis of boehmite was conventionally conducted using a high temperature (100 to 240 °C) hydrothermal process and a long reaction time (5 to 24 h) [31–33]. Metal salt such as AlCl₃, Al(NO₃)₃, Al₂(SO₄)₃ was commonly used as the metal precursor in the synthesis, using acid or base solvent such as acetic acid, NH₄OH, CO(NH₂)₂, NaOH, ethylenediamine, and triethanolamine [31–34]. In a typical-conventional procedure, boehmite particles are produced from a two-steps process: (1) dropwise addition of acid/base solution to aluminum salt solution, and (2) hydrothermal reaction at a specific high temperature with a long reaction time [31,32,34]. In this work, a green synthesis procedure of boehmite was demonstrated to substitute the conventional method. The boehmite particles were synthesized in the aqueous phase at a low temperature of 70 °C. This work aimed to characterize and investigate the adsorption properties of methionine-functionalized boehmite (MFB), which was synthesized using the one-step-green preparation technique, i.e., low temperature (70 °C) aqueous phase synthesis. The adsorption capacity enhancement due to additional functional groups from methionine was investigated toward methyl orange (MO) as the model dye.

2. Materials and Methods

2.1. Materials.

Aluminum sulfate-18-hydrate (Al₂(SO₄)₃·18H₂O, MW: 666.410 g/mol) was obtained from JT Baker, Mexico. Sodium hydroxide (NaOH, MW: 40.00 g/mol) was provided by Fisher Scientific, England. DL-Methionine (C₅H₁₁NO₂S, MW: 149.21 g/mol, 99.5%) was purchased from Sigma-Aldrich, USA. MO (C.I. 13025, C₁₄H₁₄N₃NaO₃S, MW: 327.334 g/mol) was supplied by Merck, Germany. All chemicals used in this experiment were analytical grade and directly used without any further treatment. All solutions were prepared in deionized (DI)

water, which was filtered through a NANO Pure Ultrapure water filtering system with a resistance of $18.1 \text{ M}\Omega \text{ cm}^{-1}$.

2.2. Synthesis of MFB.

Prior to the MFB synthesis, two solutions were prepared: (i) deprotonated methionine solution was prepared by adding 0.0237 mmol (3.53 g) methionine powder into 25 mL DI water containing 0.0713 mmol (2.85 g) NaOH; (ii) 0.0079 mmol (5.26 g) $\text{Al}_2(\text{SO}_4)_3 \cdot 18 \text{ H}_2\text{O}$ in 25 mL DI water. These two solutions were mixed and allowed to react at 70°C for 1 h under constant stirring. The resultant white solids (MFB) were collected by centrifugation (Hsiangtai CN-350) at 6000 rpm for 15 min and repeatedly washed with DI water until neutral pH. Those collected MFB were then dried and activated (to evaporate the H_2O bound within the material) in a vacuum oven at 100°C for 10 h. The unmodified boehmite was prepared similarly but without the addition of methionine and later was used as a control.

2.3. Characterization.

The MFB crystal pattern was recorded using a Bruker D2 Phaser-Xray Powder Diffraction equipped with a LynxEye detector and a Cu-K α radiation source with $\lambda=1.5406 \text{ \AA}$. The diffraction measurement was carried out at an angle range of 5° to 60° , with a scan step size of 0.051° . The scan time at each increment was 0.5 s. The XRD spectra were analyzed by the EVA software. Fourier transform infrared (FTIR) spectroscopy using an FTS-3500 Bio-Rad FTIR was performed to characterize the functional groups of the synthesized MFB. KBr was used as the background, and the measurements were conducted at a wavenumber range of $4000\text{--}400 \text{ cm}^{-1}$. The nitrogen adsorption-desorption experiments were carried out using a Quantachrome instrument (ASiQwin) to determine the specific surface area, pore diameter, and pore volume of MFB. Prior to the nitrogen sorption experiment, the sample was degassed, the outgassing process was operated at 100°C for 2 h. The surface topography was observed using a JSM-6500F field emission Scanning Electron Microscope (FE-SEM). Before the imaging, the samples were sputter-coated with an ultra-thin layer of conductive platinum. The backscattered electron detector at an accelerating voltage of 10 and 15 kV and a working distance (WD) of 9.4 and 11.1 mm were used for the imaging. Thermogravimetric analysis (TGA) was performed on a TA Instruments TGA 550 under N_2 flow at a constant heating rate of $10^\circ\text{C}/\text{min}$. The elemental analysis (EA) and inductively coupled plasma - optical emission spectrometry (ICP-OES) to determine the C, H, O, N, S, Na, and Al content was performed on Elementar Vario EL Cube and Thermo iCAP 7000. The point of zero charges (pH_{PZC}) was determined using a PALS Zeta Potential Analyzer (Brookhaven Instruments). The Smoluchowski model was used to obtain the zeta potential values. A series of scintillation vials containing 50 mL DI water was prepared for this analysis at different pH values (2 – 12) by adding 0.05 N NaOH or 0.05 N HCl solution. Subsequently, 10 mg of adsorbent was added to each scintillation vial and shaken with a sonicator for 1 h, and the zeta potential of each solution was measured. The pH_{PZC} was determined by plotting zeta potential values versus pH values.

2.4. Adsorption experiment.

2.4.1. Effect of pH on MO adsorption.

Before the detailed adsorption kinetic and adsorption study, the effect of pH on the adsorption efficiency of MFB for MO removal was assessed. The analysis was done according to the previous reports.[35] The initial and equilibrium concentration of MO was determined by a UV-visible spectrophotometer (UV-2600 UV-VIS Shimadzu) at 460 nm.

2.4.2. MO adsorption kinetics.

A batch adsorption kinetics experiment was conducted by adding a fixed amount of adsorbent (5 mg) into a series of scintillation vials containing 5 mL of MO solutions at various initial concentrations (9 to 60 mg L⁻¹). The adsorption was carried out in an orbital shaker incubator (DENG YNG Incubator E600L) at 200 rpm and 298 K., The amount of MO adsorbed was measured at a specific time interval. The remaining MO concentration was then determined using a spectrophotometer at a maximum wavelength of 460 nm. The amount of MO adsorbed at a specific time was determined according to Eq. (1).

$$q_t = \frac{(C_o - C_t) \times V}{m} \quad (1)$$

where C_o is the initial concentration of MO and C_t (mg L⁻¹) is the concentration of MO at a specific time t . q_t (mg g⁻¹) is the amount of MO adsorbed per g of adsorbent at a specific time. V (L) and m (g) are the volume of the adsorption system and the mass of the adsorbent, respectively.

2.4.3. MO adsorption isotherm study.

The adsorption isotherm study was conducted at various initial MO concentrations (50 to 2000 mg L⁻¹). The pH of the MO solution was adjusted to pH 3 since the best MO adsorption occurred at this pH (see the discussion section 3.3.1). The adsorbent (5 mg) was then added to the MO-containing solution. The adsorption isotherm was conducted at three different temperatures (30, 40, 50 °C) for 6 h. The amount of MO adsorbed by MFB at the equilibrium condition was calculated using Eq. (2).

$$q_e = \frac{(C_o - C_e) \times V}{m} \quad (2)$$

where C_e (mg L⁻¹) is the concentration of MO at equilibrium and q_e (mg g⁻¹) is the amount of MO adsorbed per g of adsorbent at equilibrium state.

3. Results and Discussion

3.1. The formation mechanism of MFB.

The formation of MFB was initialized by the deprotonation of methionine (Figure 1a). The deprotonation of methionine was triggered by OH⁻ ions from NaOH, which created an alkaline condition. The addition of NaOH in this step caused the increase of solution pH to 10. The deprotonation of methionine occurred at the —COOH and —NH₃⁺ groups, with pK_{a1} and pK_{a2} values of 2.16-2.28 and 9.12-9.21, respectively. The deprotonation of methionine facilitated its dissolution and allowed the formation of negatively charged methionine species [36]. Subsequently, the trivalent Al ions were added to the solution containing the deprotonated methionine. The charge difference between Al and methionine allowed the electrostatic

interaction, leading to the formation of coordinated Al/methionine complexes (Figure 1b). The excess OH⁻ ions attacked the Al metal and induced hydroxide species formation, that is, the boehmite. The methionine, initially coordinated with Al, stayed bonded with the boehmite particle, thus creating the MFB particles.

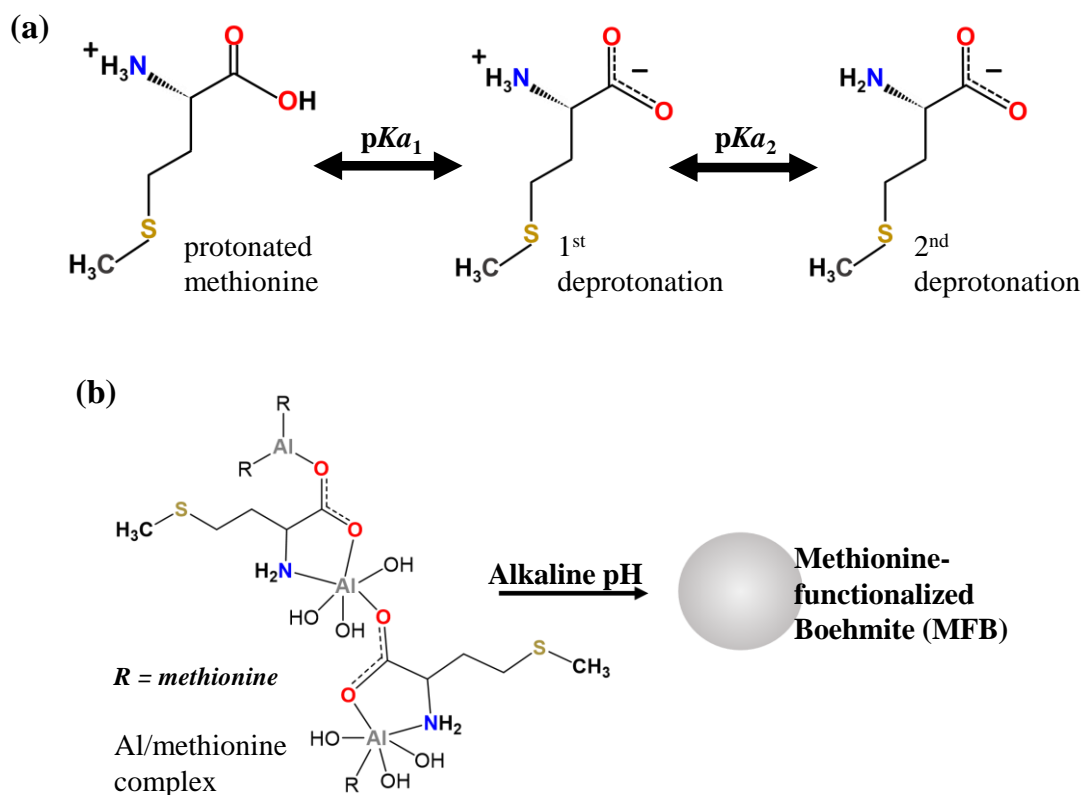


Figure 1. Schematic formation of MFB. (a) Stepwise deprotonation of methionine. (b) The formation of Al/methionine complexes, followed by the formation of methionine-functionalized boehmite (MFB) at alkaline conditions.

3.2. Characterization and compositional analysis of MFB.

3.2.1. Characterization of MFB.

The XRD crystallinity pattern of MFB particles is presented in Figure 2a. The unsharped and broad diffraction peaks of MFB indicate the amorphous nature of these particles [16]. A Rietveld refinement was conducted on the XRD pattern of MFB, and it showed good convergence with the XRD pattern of boehmite (JCPDS 21-1307). The goodness of fit was also indicated by the low Bragg R-factor (12.1) and Chi-square value (5.2) of the Rietveld refinement. The XRD pattern of the synthesized-MFB shows typical characteristic peaks at 2 θ : 14.5°, 28.6°, 38.4°, and 48.4°, corresponding to the (020), (021), (130), and (150) crystal plane, respectively [37]. This result demonstrates that γ -AlO(OH) is the major crystal component in the MFB compound.

The FTIR spectra bands of MFB are shown in Figure 2b. The asymmetric and symmetric stretching vibrations of the —OH group were indicated by the appearance of bands at 3390 and 3102 cm⁻¹, respectively. Meanwhile, the symmetric bending vibration of —OH was indicated by the band at 1068 cm⁻¹. The presence of coordinated Al-O was indicated by bands at 747, 646, and 486 cm⁻¹ [38]. Evidence of methionine binding in MFB was indicated by the appearance of methionine characteristic peaks [39], such as CH₃ stretching vibration at

2922 and 2835 cm^{-1} , C=O stretching at 2094 and 1687 cm^{-1} , C-N stretching at 1424 cm^{-1} , and CH_2 -S wagging vibration at 1220 cm^{-1} .

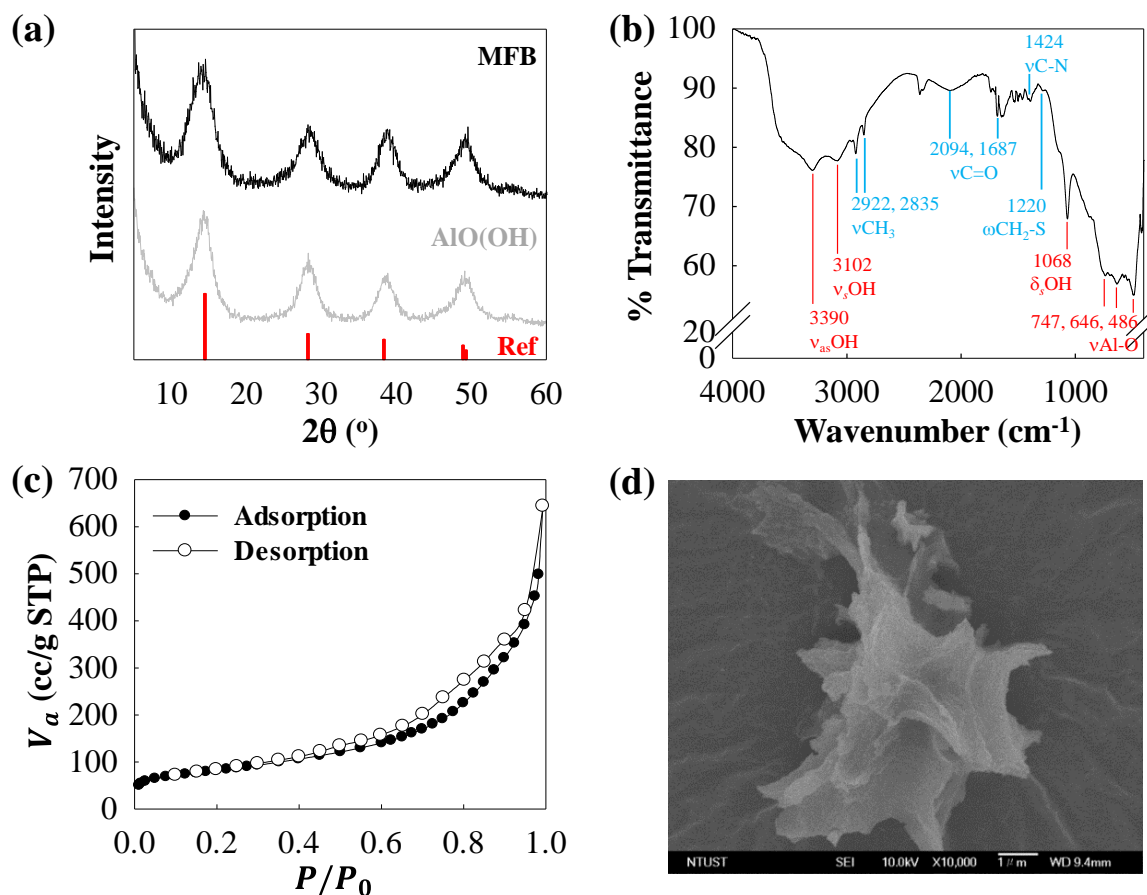


Figure 2. Characterization of MFB. (a) XRD pattern of MFB. The XRD reference pattern of γ -AlO(OH) was adopted from JCPDS 21-1307 (gray plot). (b) FTIR chromatogram of MFB with characteristic peaks of γ -AlO(OH) and methionine are labeled in red and blue color, respectively. (c) N_2 adsorption-desorption isotherm of MFB. (d) SEM image of MFB.

The N_2 sorption isotherm curves of MFB are shown in Figure 2c. A typical type-IV mannerism with a broad hysteresis loop at a relative pressure (P/P_0) between 0.4 to 1.0, indicates the mesoporous structure of MFB. The steep gradient in the hysteresis loop denotes capillary condensation, which causes a delayed desorption process [40]. Calculation using the BJH equation further confirms the mesoporous structure with an average pore diameter of 13.85 nm. The calculated BET surface area and total pore volume of MFB are $287 \text{ m}^2 \text{ g}^{-1}$ and $0.996 \text{ cm}^3 \text{ g}^{-1}$, respectively.

The SEM image of MFB (Figure 2d) shows the morphology of the particles. No specific geometry can be observed from the particles. The particles show an irregular surface characteristic that resembles a crumpled sheet.

3.2.2. Compositional analysis of MFB.

The composition and quantity of the content in the MFB were determined by TGA and EA. The result of the TGA analysis is shown in Figure 3. The decomposition of the MFB material is divided into three stages. The first stage is a sharp decrease of around 9% of mass loss from room temperature until $\sim 100^\circ\text{C}$. At this stage, the H_2O in the material has evaporated and marked the desorption of physic-sorb. Subsequently, the second stage of the decline is

wider from 100 to 500°C with 20% mass loss, and this condition is the result of the transformation MFB change into γ -alumina. From this stage, it was explained that the amount of methionine contained in the MFB was about 20% by mass. The last stage portrayed no significant decrease of mass from 500 to 900°C with 3.3% mass loss, and this result connected to the elimination of residual hydroxyls (-OH). After 900°C, the remaining component is Al_2O_3 [41]. The EA data (C 0.36, H 3.75, O 30.32, Al 57.14, Na 4.76, and trace amount of N, S) are consistent with the TGA result, where the major component in the MFB material is Al and O.

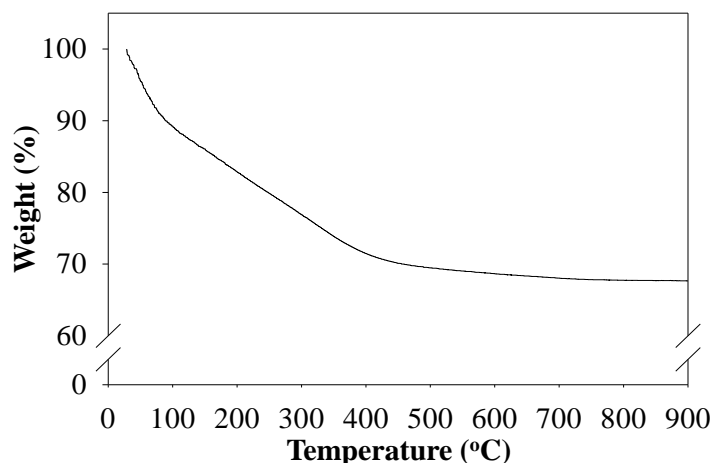


Figure 3. TGA analysis of MFB.

3.3. Adsorption of MO by MFB.

3.3.1. Compares Adsorption of MO by Boehmite and MFB.

The success in boehmite modification by methionine also can be observed by the enhanced adsorption capacity of MFB compared to the unmodified boehmite. As shown in Table 1, the MFB showed a 1.33-fold higher adsorption capacity than the unmodified one. This suggests that the amine group of methionine may facilitate a selective binding affinity towards anionic dyes such as MO.

Table 1. Adsorption of MO at 25°C.

Adsorbent	q_e (mg g ⁻¹)
Boehmite *	32.68 ± 0.59
MFB	43.48 ± 0.42

* without methionine functionalization

3.3.2. Effect of pH.

As shown in Figure 4a, maximum adsorption of MO by MFB occurred at pH 3. Adsorption of MO decreased sharply as the pH was increased to >4. This phenomenon can be explained by the surface charge of the MFB particles and the charge of MO molecules. At acidic pH, the excess H^+ ions attack the MFB particles (Al-OH and Al-NH_2) and cause positive surface charges (Al-OH_2^+ and Al-NH_3^+). The sulphonate group (SO_3^-) of the MO are willingly dissociated to form the anion. The positively charged MFB particles at acidic pH were confirmed from the positive zeta potential value, as shown in Figure 4b. MO, which is an anionic dye, is attracted to the MFB particles due to the difference in charge. Therefore, the electrostatic interaction occurs, leading to the attachment of MO on MFB [42,43]. As the pH increases, the zeta potential of MFB decreases toward the negative value. Thus, the electrostatic attraction between the two compounds is reduced as the surface charges become more negative.

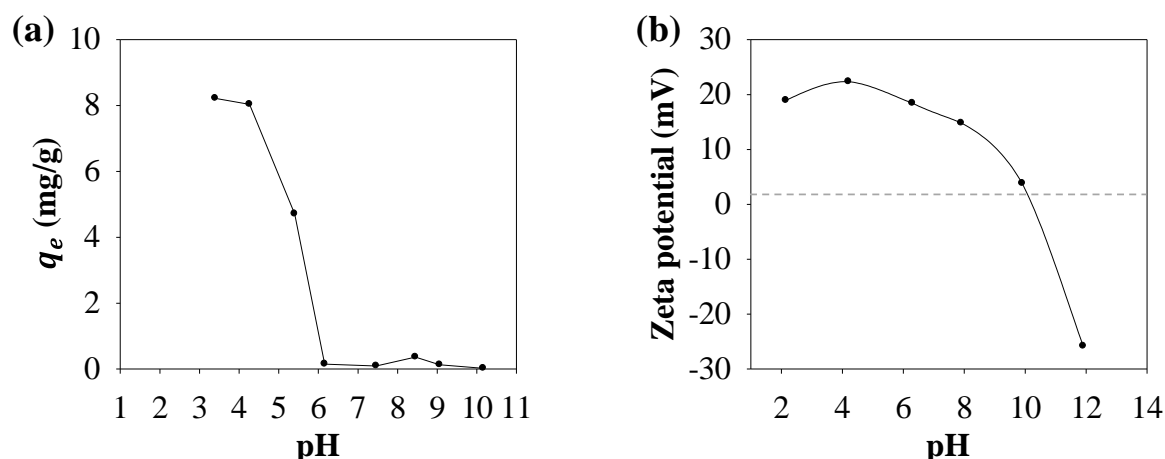


Figure 4. Effect of pH on MFB adsorption efficiency and surface property. (a) Adsorption capacity (q_e , mg/g) of MFB for MO removal and (b) Zeta potential of MFB from pH 3 to 10.

3.3.3. Adsorption kinetics.

Adsorption kinetics plays an important role in providing information about the time required to reach equilibrium [44]. As shown in Figure 5, rapid uptake of MO occurred in the first 15 min. A deceleration point before the plateau occurred at $t = 30$ min. The kinetics data were fitted with the pseudo-first-order by Lagergren [45] and pseudo-second-order [46] models to determine the adsorption rates. The corresponding mathematical expression of the two models is presented as Eq. (3) and (4), respectively.

$$q_t = q_{e1}(1 - e^{-k_1 t}) \quad (3)$$

$$q_t = \frac{q_{e2}^2 k_2 t}{1 + k_2 q_{e2} t} \quad (4)$$

where $k_1(\text{min}^{-1})$ and $k_2(\text{g mg}^{-1} \text{min}^{-1})$ are the first- and second-order rate constants, respectively.

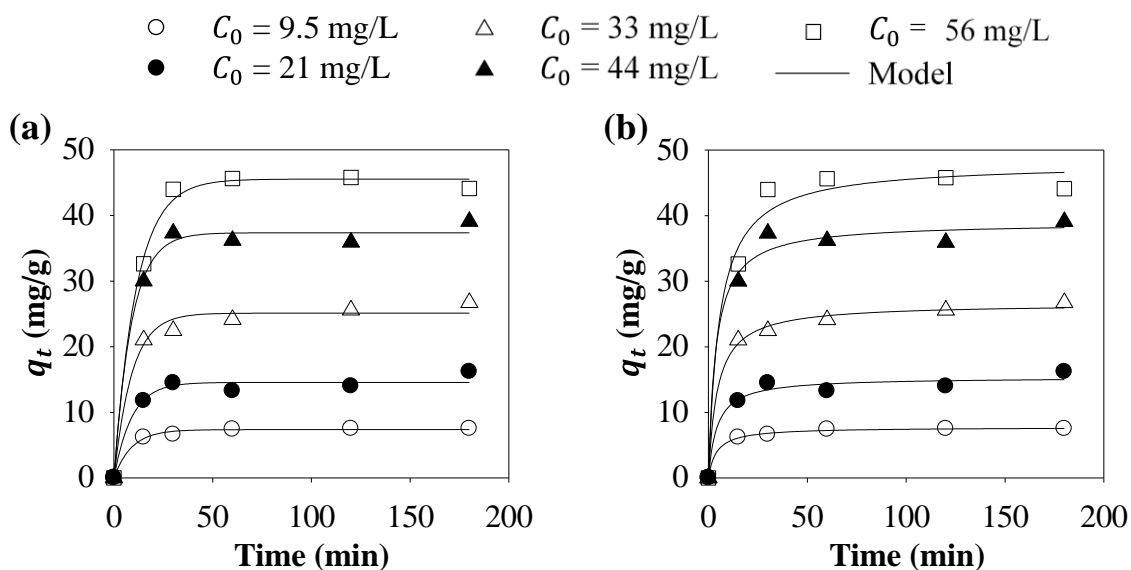


Figure 5. Adsorption kinetics of MO onto MFB. Solid lines represent (a) pseudo-first-order and (b) pseudo-second-order fitting curves.

The calculated kinetic parameters obtained from the data fitting are shown in Table 2. The values of q_e from the pseudo-first-order model are very close to the experimental data

($q_{e,exp}$), indicating that this model can satisfactorily represent the kinetics data. The goodness of fit of the pseudo-first-order model is also indicated by their correlation coefficients value (R^2) which close to 1. The effect of increasing initial MO concentration (C_0) on the parameters q_e and k was also observed. A high C_0 induces higher MO uptake, as indicated by the higher q_e . This is since a higher number of adsorbate molecules can provide a higher driving force to overcome the mass transfer resistance. In contrast, the increase in C_0 is followed by a decrease in adsorption rate (k). The decline of k at higher C_0 is attributed to the higher probability of collisions between molecules which cause an increase in mobility of the molecules and prevent the adsorbates from attaching to the adsorbent surface [35,47].

Table 2. Summarize of kinetic parameters of MO onto MFB material at 25°C

	The initial concentration of MO (mg/L)				
	9.5	21	33	44	56
$q_{e,exp}$ (mg/g)	7.5128	16.1943	26.7279	39.0902	45.8017
Pseudo-first order					
q_{e1} (mg g ⁻¹)	7.3690	14.5701	25.1250	37.1854	45.5491
k_1 (min ⁻¹)	0.1118	0.1120	0.1105	0.1668	0.0888
R^2	0.9922	0.9715	0.9856	0.9944	0.9965
Pseudo-second order					
q_{e2} (mg g ⁻¹)	7.7335	15.3584	26.5935	38.9599	48.0305
k_2 (g mg ⁻¹ min ⁻¹)	0.0322	0.0153	0.0084	0.0069	0.0038
R^2	0.9981	0.9741	0.9966	0.9882	0.9835

3.3.4. Adsorption isotherms and thermodynamic.

The Langmuir and Freundlich models were used to represent the adsorption equilibria of MO on MFB. The Langmuir isotherm model has the form as follows.

$$q_e = \frac{K_L Q_m C_e}{1 + K_L C_e} \quad (5)$$

where Q_m (mg g⁻¹) and K_L (L mg⁻¹) are adsorption capacity and adsorption affinity, respectively.

Hall et al. (1966) and Tran et al. (2017) suggested that the separation factor or equilibrium parameter (R_L) can be used to express the essential characteristics of the Langmuir isotherm. The R_L value which describes the adsorption favorability, wherein $R_L < 1$ shows favorable adsorption and $R_L > 1$ shows unfavorable adsorption [44,48]. R_L is a dimensionless constant and is defined as follows:

$$R_L = \frac{1}{1 + K_L C_0} \quad (6)$$

The Freundlich isotherm has a mathematical form shown in Eq. (7).

$$q_e = K_F C_e^{1/n} \quad (7)$$

where K_F ((mg/g)/(mg/L)ⁿ) and n (dimensionless) are Freundlich adsorption capacity and the intensity parameter, respectively.

The adsorption isotherm data and the fitting are depicted in Figure 6. According to the classification by Giles et al. (1960), the adsorption isotherm curve can be classified as an L-curve with subclass 1 [49]. The L-type curve indicates that the adsorption occurs mainly due to the weak forces, i.e., van der Waals forces. Subclass 1 suggests that the adsorption sites were not fully occupied. Due to MFB have large capacity: surface area and total pore volume (287 m² g⁻¹ and 0.996 cm³ g⁻¹, respectively).

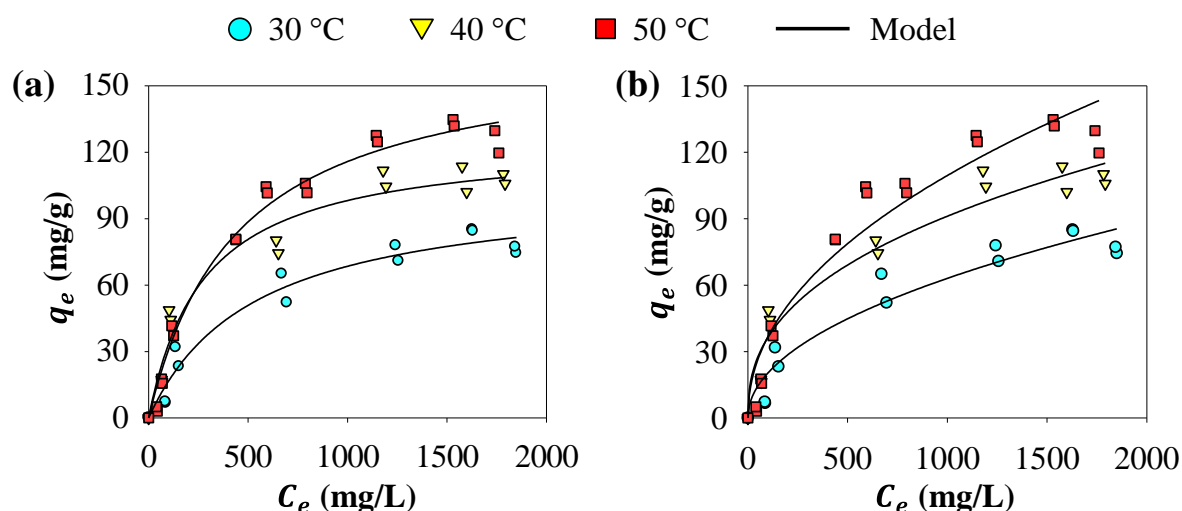


Figure 6. Adsorption isotherm of MO onto MFB at different temperatures. Solid lines represent (a) Langmuir and (b) Freundlich fitting curves.

All constants obtained from the two isotherm models are summarized in Table 3. Based on the correlation coefficient (R^2), the Langmuir model is more suitable than the Freundlich model. In this study, the temperature positively influenced the amount of MO adsorbed by MFB. Increasing temperature from 303 to 323 K resulted in the increase of Q_m from 104.9140 to 167.4075 mg g⁻¹. Based on the separation factor or equilibrium parameter (R_L), this adsorption is favorable because of $R_L < 1$ [44].

Table 3. Summary of the temperature effects on adsorption isotherm parameters of MO onto MFB material

Temperature (K)	Langmuir				Freundlich		
	Q_m (mg/g)	K_L (L/mg)	R^2	R_L	K_F (mg/g)(mg/L) ^{1/n}	$1/n$	R^2
303	104.9140	0.0019	0.9613	0.21-0.84	2.0902	0.4932	0.9346
313	125.5011	0.0036	0.9595	0.12-0.73	5.7638	0.3997	0.9492
323	167.4075	0.0022	0.9827	0.19-0.90	4.0792	0.4763	0.9361

The thermodynamic adsorption parameters were determined based on Eq. (8) and (9).

$$\Delta G = -RT \ln(K_C) \quad (8)$$

where ΔG (kJ mol⁻¹), R (8.3144 J mol⁻¹ K⁻¹), T (K), and K_C (dimensionless) are the change in Gibbs free energy, the ideal gas constant, the temperature of the process, and the equilibrium constant, respectively. The K_C value can be obtained by multiplying K_L (L mg⁻¹) value with the molecular weight of the adsorbate (g mol⁻¹) and by 55.5, which corresponds to the number of moles of pure water per liter [50]. The van't Hoff equation, Eq. (9), was then used to determine the change in enthalpy (ΔH , kJ mol⁻¹) and entropy (ΔS , J mol⁻¹ K⁻¹).

$$\Delta G = \Delta H - T\Delta S \quad (9)$$

Table 4. Thermodynamic properties of adsorption of MO onto MFB.

Temperature (K)	ΔG° (kJ mol ⁻¹)	ΔH (kJ mol ⁻¹)	ΔS (J mol ⁻¹ K ⁻¹)
303	-26.3243	6.4528	109.6836
313	-28.8562		
323	-28.4556		

The obtained thermodynamic parameters are summarized in Table 4. The negative ΔG values of -26.3243, -28.8562, and -28.4556 kJ mol⁻¹ were obtained for adsorption at 303, 313, and 323 K, respectively. The increase in temperature followed by a decrease in ΔG value

indicates the spontaneity of the adsorption. The calculated ΔH value is $+6.4528 \text{ kJ mol}^{-1}$, which shows the occurrence of an endothermic process. Meanwhile, the positive value of ΔS ($109.6836 \text{ J mol}^{-1} \text{ K}^{-1}$) indicates the increase of randomness during MO uptake onto MFB [51].

3.3.5. Adsorption mechanism.

FTIR and XRD measurements were employed on the spent-MFB (MO@MFB) to gain insight into the adsorption mechanism of MO onto the adsorbent. As shown in Figure 7a, there is a change in the bands at about 3500 cm^{-1} , corresponding to the —OH group vibration. The band alteration can be attributed to the interaction between the MO molecules and the —OH group on the surface of MFB, which occurred through the van der Waals interactions. Another band change was observed at $\sim 2900 \text{ cm}^{-1}$, corresponding to the CH_3 alkyl group vibration [52]. These results suggest that there was an interaction between the MO molecules with the alkyl group. However, there is no significant change in the XRD spectra of MO@MFB from that of MFB, which implies that there is no molecular structure change due to the attachment of MO (Figure 7b). Overall, the FTIR and XRD data indicate that the adsorption of MO by MFB does not occur via anion-cation exchange [16] but through a physical process.

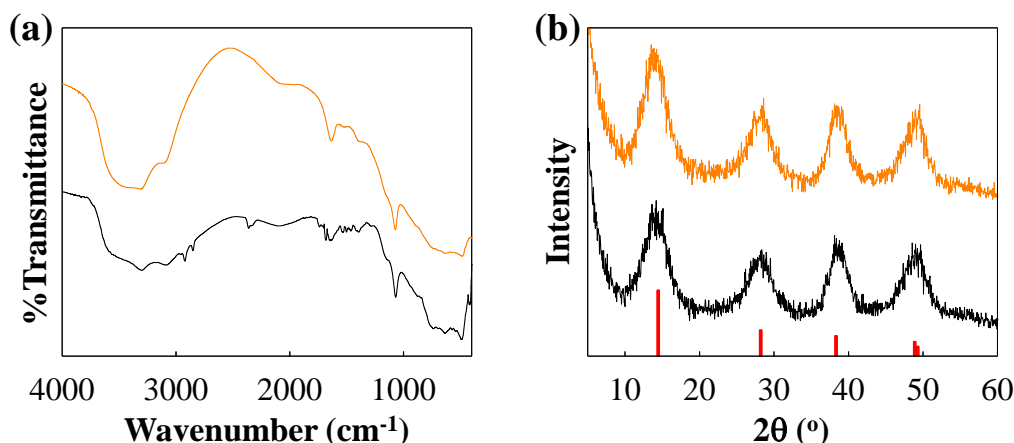


Figure 7. Characterization of MFB after adsorption of MO (MO@MFB). (a) FTIR spectra and (b) XRD pattern of MFB (black color) and MO@MFB (orange color).

Table 5 compares the maximum adsorption capacity (Q_m) of MFB (in this work) and several functionalized-adsorbent for MO removal. The Q_m of MFB was ~ 20.9 -folds higher than that of the unmodified boehmite ($\gamma\text{-AlO(OH)}$). MFB also shows much higher MO adsorption (~ 10.8 times) than the amino-crosslinked hypromellose. On the other hand, the Q_m of MFB was about 11% lower than the amino-MIL-101(Al). Furthermore, the use of MFB offers several advantages in terms of its synthesis procedure. MFB can be synthesized at a lower temperature within a shorter duration than the other adsorbents listed in Table 5, thus providing an economic incentive for MFB.

Table 5. MO adsorption capacity by amine-composite materials.

Material	Synthesis condition	Q_m (mg/g)	Reference
Amino-MIL-101(Al)	130°C, 6 h	188.00	[53]
Amino-crosslinked hypromellose	80°C, 3 h	15.56	[54]
$\gamma\text{-AlO(OH)}$	150°C, 24 h	8.00	[34]
MFB	70°C, 1 h	167.41	This work

4. Conclusions

A green and energy-efficient technique was demonstrated to synthesize methionine-functionalized boehmite in an aqueous phase at a low temperature of 70°C. Methionine act as the Al complexation ligand that facilitates the formation of the Al-oxide-hydroxide (boehmite). The presence of methionine provides additional surface binding sites of boehmite, which enhances its adsorption capacity. The adsorption study of the methionine-functionalized boehmite against MO showed that the adsorption between the two compounds occurred via van der Waals forces. The adsorption proceeded more spontaneously at a higher temperature, indicating the endothermic nature of the adsorption process.

Funding

Financial support by the National Science Council of Taiwan (MOST 108-2221-E-011-106) is appreciated. A.E. Angkawijaya and A.W. Go would like to thank the National Taiwan University of Science and Technology for the teaching and research start-up support and grant provided for 2019–2021 to organize the research group involved in this work.

Acknowledgments

This research has no acknowledgment.

Conflicts of Interest

The authors declare that the research was conducted without any commercial or financial relationships that could be construed as a potential conflict of interest.

References

1. Zhao, N.; Sun, F.; Li, P.; Mu, X.; Zhu, G. An Amino-Coordinated Metal-Organic Framework for Selective Gas adsorption. *Inorganic Chemistry* **2017**, *56*, 6938–6942, <https://doi.org/10.1021/acs.inorgchem.7b00436>.
2. Hu, J.; Yu, H.; Dai, W.; Yan, X.; Hu, X.; Huang, H. Enhanced adsorptive removal of hazardous anionic dye “congo red” by a Ni/Cu mixed-component metal–organic porous material. *RSC Advances* **2014**, *4*, 35124–35130, <https://doi.org/10.1039/C4RA05772D>.
3. Velusamy, S.; Roy, A.; Sundaram, S.; Kumar Mallick, T. A Review on Heavy Metal Ions and Containing Dyes Removal Through Graphene Oxide-Based Adsorption Strategies for Textile Wastewater Treatment. *Chem Rec* **2021**, *21*, 1570–1610, <https://doi.org/10.1002/tcr.202000153>.
4. Gupta, V.K.; Jain, R.; Nayak, A.; Agarwal, S.; Shrivastava, M. Removal of the hazardous dye—Tartrazine by photodegradation on titanium dioxide surface. *Materials Science and Engineering: C* **2011**, *31*, 1062–1067, <https://doi.org/10.1016/j.msec.2011.03.006>.
5. Liu, L.; Zhang, B.; Zhang, Y.; He, Y.; Huang, L.; Tan, S.; Cai, X. Simultaneous removal of cationic and anionic dyes from environmental water using montmorillonite-pillared graphene oxide. *Journal of Chemical and Engineering Data* **2015**, *60*, 1270–1278, <https://doi.org/10.1021/je5009312>.
6. Azhar, B.; Angkawijaya, A.E.; Santoso, S.P.; Gunarto, C.; Ayucitra, A.; Go, A.W.; Tran-Nguyen, P.L.; Ismadji, S.; Ju, Y.-H. Aqueous synthesis of highly adsorptive copper–gallic acid metal–organic framework. *Scientific Reports* **2020**, *10*, <https://doi.org/10.1038/s41598-020-75927-4>.
7. Putri, M.; Lou, C.-H.; Syai'in, M.; Ou, S.-H.; Wang, Y.-C. Long-Term River Water Quality Trends and Pollution Source Apportionment in Taiwan. *Water* **2018**, *10*, <https://doi.org/10.3390/w10101394>.
8. Elbasiouny, H.; Darwesh, M.; Elbeltagy, H.; Abo-Alhamd, F.G.; Amer, A.A.; Elsegaay, M.A.; Khattab, I.A.; Elsharawy, E.A.; Ebehiry, F.; El-Ramady, H.; Brevik, E.C. Ecofriendly remediation technologies for wastewater contaminated with heavy metals with special focus on using water hyacinth and black tea wastes: a review. *Environ Monit Assess* **2021**, *193*, <https://doi.org/10.1007/s10661-021-09236-2>.
9. Cabral, J.B.P.; Nogueira, P.F.; Becegato, V.A.; Becegato, V.R.; Paulino, A.T. Environmental Assessment and Toxic Metal-Contamination Level in Surface Sediment of a Water Reservoir in the Brazilian Cerrado. *Water* **2021**, *13*, <https://doi.org/10.3390/w13081044>.

10. Stone, C.; Windsor, F.M.; Munday, M.; Durance, I. Natural or synthetic – how global trends in textile usage threaten freshwater environments. *Science of The Total Environment* **2020**, *718*, <https://doi.org/10.1016/j.scitotenv.2019.134689>.
11. Lellis, B.; Fávaro-Polonio, C.Z.; Pamphile, J.A.; Polonio, J.C. Effects of textile dyes on health and the environment and bioremediation potential of living organisms. *Biotechnology Research and Innovation* **2019**, *3*, 275-290, <https://doi.org/10.1016/j.biori.2019.09.001>.
12. El-Ahmady El-Naggar, N.; Rabei, N.H.; El-Malkey, S.E. Eco-friendly approach for biosorption of Pb(2+) and carcinogenic Congo red dye from binary solution onto sustainable *Ulva lactuca* biomass. *Sci Rep* **2020**, *10*, <https://doi.org/10.1038/s41598-020-73031-1>.
13. Ceretta, M.B.; Nercessian, D.; Wolski, E.A. Current Trends on Role of Biological Treatment in Integrated Treatment Technologies of Textile Wastewater. *Front Microbiol* **2021**, *12*, <https://doi.org/10.3389/fmicb.2021.651025>.
14. Ardila-Leal, L.D.; Poutou-Pinales, R.A.; Pedroza-Rodriguez, A.M.; Quevedo-Hidalgo, B.E. A Brief History of Colour, the Environmental Impact of Synthetic Dyes and Removal by Using Laccases. *Molecules* **2021**, *26*, <https://doi.org/10.3390/molecules26133813>.
15. Katheresan, V.; Kansedo, J.; Lau, S.Y. Efficiency of various recent wastewater dye removal methods: A review. *Journal of Environmental Chemical Engineering* **2018**, *6*, 4676-4697, <https://doi.org/10.1016/j.jece.2018.06.060>.
16. Gao, Y.; Deng, S.-Q.; Jin, X.; Cai, S.-L.; Zheng, S.-R.; Zhang, W.-G. The construction of amorphous metal-organic cage-based solid for rapid dye adsorption and time-dependent dye separation from water *Chemical Engineering Journal* **2019**, *357*, 129-139, <https://doi.org/10.1016/j.cej.2018.09.124>.
17. Pishnamazi, M.; Khan, A.; Kurniawan, T.A.; Sanaeepur, H.; Albadarin, A.B.; Soltani, R. Adsorption of dyes on multifunctionalized nano-silica KCC-1. *Journal of Molecular Liquids* **2021**, *338*, <https://doi.org/10.1016/j.molliq.2021.116573>.
18. Kinoshita, Y.; Shimoyama, Y.; Masui, Y.; Kawahara, Y.; Arai, K.; Motohashi, T.; Noda, Y.; Uchida, S. Amorphous High-Surface-Area Aluminum Hydroxide–Bicarbonates for Highly Efficient Methyl Orange Removal from Water. *Langmuir* **2020**, *36*, 6277-6285, <https://doi.org/10.1021/acs.langmuir.0c00021>.
19. Weidner, E.; Ciesielczyk, F. Removal of Hazardous Oxyanions from the Environment Using Metal-Oxide-Based Materials *Materials* **2019**, *12*, 927-958, <https://doi.org/10.3390/ma12060927>.
20. Wang, L.; Shi, C.; Wang, L.; Pan, L.; Zhang, X.; Zou, J.-J. Rational design, synthesis, adsorption principles and applications of metal oxide adsorbents: a review. *Nanoscale* **2020**, *12*, 4790-4815, <https://doi.org/10.1039/C9NR09274A>.
21. Takagaki, A.; Jung, J.C.; Hayashi, S. Solid Lewis acidity of boehmite AlO(OH) and its catalytic activity for transformation of sugars in water. *The Royal Society of Chemistry Advances* **2014**, *4*, 43785-43791, <https://doi.org/10.1039/C4RA08061K>.
22. Lueangchaichaweng, W.; Singh, B.; Mandelli, D.; Carvalho, W.A.; Fiorilli, S.; Pescarmona, P.P. High surface area, nanostructured boehmite and alumina catalysts: Synthesis and application in the sustainable epoxidation of alkenes. *Applied Catalysis A, General* **2019**, *571*, 180-187, <https://doi.org/10.1016/j.apcata.2018.12.017>.
23. Kumar, C.S.; Hareesh, U.S.; Damodaran, A.D.; Warner, K.G.K. Monohydroxy Aluminium Oxide (Boehmite, AlOOH) as a Reactive Binder for Extrusion of Alumina Ceramics *Journal of the European Ceramic Society* **1997**, *17*, 1167-1172, [https://doi.org/10.1016/S0955-2219\(96\)00214-2](https://doi.org/10.1016/S0955-2219(96)00214-2).
24. Boccacini, A.R.; Kaya, C. Alumina ceramics based on seeded boehmite and electrophoretic deposition. *Ceramics International* **2002**, *28*, 893-897, [https://doi.org/10.1016/S0272-8842\(02\)00070-6](https://doi.org/10.1016/S0272-8842(02)00070-6).
25. Yilmaz, O.; Buytoz, S. Abrasive wear of Al₂O₃-reinforced aluminium-based MMCs. *Composites Science and Technology* **2001**, *61*, 2381-2392, [https://doi.org/10.1016/S0266-3538\(01\)00131-2](https://doi.org/10.1016/S0266-3538(01)00131-2).
26. Bao, S.; Syvertsen, M.; Kvithyld, A.; Engh, T. Wetting behavior of aluminium and filtration with Al₂O₃ and SiC ceramic foam filters *Trans. Nonferrous Met. Soc. China* **2014**, *24*, 3922-3928, [https://doi.org/10.1016/S1003-6326\(14\)63552-4](https://doi.org/10.1016/S1003-6326(14)63552-4).
27. Elwakeel, K.Z.; Elgarahy, A.M.; Khan, Z.A.; Almughamisi, M.S.; Al-Bogami, A.S. Perspectives regarding metal/mineral-incorporating materials for water purification: with special focus on Cr(vi) removal. *Materials Advances* **2020**, *1*, 1546-1574, <https://doi.org/10.1039/D0MA00153H>.
28. Rajamani, M.; Rajendrakumar, K. Chitosan-boehmite desiccant composite as a promising adsorbent towards heavy metal removal. *Journal of Environmental Management* **2019**, *244*, 257-264, <https://doi.org/10.1016/j.jenvman.2019.05.056>.
29. Imaz, I.; Rubio-Martinez, M.; An, J.; Sole-Font, I.; Rosi, N.L.; MasPOCH, D. Metal-biomolecule frameworks *Chem. Commun.* **2011**, *47*, 7287-7302, <https://doi.org/10.1039/c1cc11202c>.
30. Qamar, N.; Sultan, H.; Khan, K.M.; Azmat, R.; Naz, R.; Hameed, A.; Lateef, M. 8-Hydroxyquinoline-Methionine Mixed Ligands Metal Complexes: Preparation and Their Antioxidant Activity. *Chemistry Select* **2019**, *4*, 3058-3061, <https://doi.org/10.1002/slct.201803882>.
31. He, T.; Xiang, L.; Zhu, S. Different Nanostructures of Boehmite Fabricated by Hydrothermal Process: Effects of pH and Anions. *The Royal Society of Chemistry Cryst. Eng. Comm.* **2009**, *11*, 1338-1342, <https://doi.org/10.1039/B900447P>.

32. Liu, L.; Zhao, J.; Zhang, Y.; Zhao, F.; Zhang, Y. Fabrication of superhydrophobic surface by hierarchical growth of lotus-leaf-like boehmite on aluminum foil *Journal of Colloid and Interface Science* **2011**, *358*, 277-283, <https://doi.org/10.1016/j.jcis.2011.02.036>.
33. Zhao, Z.-G.; Nagai, N.; Kodaira, T.; Hukuta, Y.; Bando, K.; Takashima, H.; Mizukami, F. Surface treatment and calcination temperature-dependent adsorption of methyl orange molecules in wastewater on self-standing alumina nanofiber films. *J. Mater. Chem.* **2011**, *21*, 14984-14989, <https://doi.org/10.1039/C1JM12241J>.
34. Xiao, J.; Ji, H.; Shen, Z.; Yang, W.; Guo, C.; Wang, S.; Zhang, X.; Fu, R.; Ling, F. Self-assembly of flower-like AlOOH and Al₂O₃ with hierarchical nanoarchitectures and enhanced adsorption performance towards methyl orange *Royal Society of Chemistry Advances* **2014**, *4*, 35077-35083, <https://doi.org/10.1039/C4RA05343E>.
35. Angkawijaya, A.E.; Santoso, S.P.; Bundjaja, V.; Soetaredjo, F.E.; Gunarto, C.; Ayucitra, A.; Ju, Y.-H.; Go, A.W.; Ismadji, S. Studies on the performance of bentonite and its composite as phosphate adsorbent and phosphate supplementation for plant. *Journal of Hazardous Materials* **2020**, *399*, <https://doi.org/10.1016/j.jhazmat.2020.123130>.
36. Kayal, S.; Chakraborty, A.; Teo, H.W.B. Green synthesis and characterization of aluminium fumarate metal-organic framework for heat transformation applications. *Materials Letters* **2018**, *221*, 165-167, <https://doi.org/10.1016/j.matlet.2018.03.099>.
37. Djošić, M.S.; Mišković-Stanković, V.B.; Janačković, D.T.; Kačarević-Popović, Z.M.; Petrović, R.D. Electrophoretic deposition and characterization of boehmite coatings on titanium substrate. *Colloids and Surfaces A: Physicochemical and Engineering Aspects* **2006**, *274*, 185-191, <https://doi.org/10.1016/j.colsurfa.2005.08.048>.
38. Kiss, A.B.; Keresztury, G.; Farkas, L. Raman and i.r. spectra and structure of boehmite (γ -AlOOH). Evidence for the recently discarded D172h space group. *Spectrochimica Acta Part A: Molecular Spectroscopy* **1980**, *36*, 653-658, [https://doi.org/10.1016/0584-8539\(80\)80024-9](https://doi.org/10.1016/0584-8539(80)80024-9).
39. Ramachandran, E.; Natarajan, S. Gel growth and characterization of β -DL-methionine. *Crystal Research and Technology* **2006**, *41*, 411-415, <https://doi.org/10.1002/crat.200510595>.
40. Ismadji, S.; Sudaryanto, Y.; Hartono, S.B.; Setiawan, L.E.K.; Ayucitra, A. Activated carbon from char obtained from vacuum pyrolysis of teak sawdust: pore structure development and characterization. *Bioresource Technology* **2005**, *96*, 1364-1369, <https://doi.org/10.1016/j.biortech.2004.11.007>.
41. Alphonse, P.; Courty, M. Structure and thermal behavior of nanocrystalline boehmite. *Thermochimica Acta* **2005**, *425*, 75-89, <https://doi.org/10.1016/j.tca.2004.06.009>.
42. Carpio, I.E.M.; Mangadlao, J.D.; Nguyen, H.N.; Advincula, R.C.; Rodrigues, D.F. Graphene oxide functionalized with ethylenediamine triacetic acid for heavy metal adsorption and anti-microbial applications. *Carbon* **2014**, *77*, 289-301, <https://doi.org/10.1016/j.carbon.2014.05.032>.
43. Jiang, Y.; Gong, J.-L.; Zeng, G.-M.; Ou, X.-M.; Chang, Y.-N.; Deng, C.-H.; Zhang, J.; Liu, H.-Y.; Huang, S.-Y. Magnetic chitosan-graphene oxide composite for anti-microbial and dye removal applications. *International Journal of Biological Macromolecules* **2016**, *82*, 702-710, <https://doi.org/10.1016/j.ijbiomac.2015.11.021>.
44. Tran, H.N.; You, S.-J.; Hosseini-Bandegharai, A. Mistakes and inconsistencies regarding adsorption of contaminants from aqueous solutions: A critical review. *Water Research* **2017**, *120*, 88-116, <https://doi.org/10.1016/j.watres.2017.04.014>.
45. Tien, C.; Ramarao, B.V. On the significance and utility of the Lagergren model and the pseudo second-order model of batch adsorption. *Separation Science and Technology* **2017**, *52*, 975-986, <https://doi.org/10.1080/01496395.2016.1274327>.
46. Blanchard, G.; Maunaye, M.; Martin, G. Removal of heavy metals from waters by means of natural zeolites. *Water Res.* **1984**, *18*, 1501-1507, [https://doi.org/10.1016/0043-1354\(84\)90124-6](https://doi.org/10.1016/0043-1354(84)90124-6).
47. Lim, A.; Chew, J.J.; Ngu, L.H.; Ismadji, S.; Khaerudini, D.S.; Sunarso, J. Synthesis, Characterization, Adsorption Isotherm, and Kinetic Study of Oil Palm Trunk-Derived Activated Carbon for Tannin Removal from Aqueous Solution. *ACS Omega* **2020**, *5*, 28673-28683, <https://doi.org/10.1021/acsomega.0c03811>.
48. Hall, K.R.; Eagleton, L.C.; Acrivos, A.; Vermeulen, T. Pore and solid-diffusion kinetics in fixed-bed adsorption under constant-pattern conditions *Ind. Eng. Chem. Fundam.* **1966**, *5*, 212-223, <https://doi.org/10.1021/i160018a011>.
49. Giles, C.H.; MacEwan, T.H.; Nakhwa, S.N.; Smith, D. 786. Studies in adsorption. Part XI. A system of classification of solution adsorption isotherms, and its use in diagnosis of adsorption mechanisms and in measurement of specific surface areas of solids. *Journal of the Chemical Society (Resumed)* **1960**, *1960*, 3973-3993, <https://doi.org/10.1039/JR9600003973>.
50. Zhou, X.; Zhou, X. The unit problem in the thermodynamic calculation of adsorption using the Langmuir equation *Chem. Eng. Commun.* **2014**, *201*, 1459-1467, <https://doi.org/10.1080/00986445.2013.818541>.
51. Ke, F.; Peng, C.; Zhang, T.; Zhang, M.; Zhou, C.; Cai, H.; Zhu, J.; Wan, X. Fumarate-based metal-organic frameworks as a new platform for highly selective removal of fluoride from brick tea. *Scientific Reports* **2018**, *8*, 1-11, <https://doi.org/10.1038/s41598-018-19277-2>.

52. Allouche, F.-N.; Yassaa, N.; Lounici, H. Sorption of Methyl Orange from Aqueous Solution on Chitosan Biomass. *Procedia Earth and Planetary Science* **2015**, *15*, 596-601, <https://doi.org/10.1016/j.proeps.2015.08.109>.
53. Haque, E.; Lo, V.; Minett, A.I.; Harris, A.T.; Church, T.L. Dichotomous adsorption behaviour of dyes on an amino-functionalised metal-organic framework, amino-MIL-101(Al). *Journal of Materials Chemistry A* **2014**, *2*, 193-203, <https://doi.org/10.1039/C3TA13589F>.
54. Qu, W.; He, D.; Huang, H.; Guo, Y.; Tang, Y.; Song, R.-J. Characterization of amino-crosslinked hypromellose and its adsorption characteristics for methyl orange from water. *Journal of Materials Science* **2020**, *55*, 7268-7282, <https://doi.org/10.1007/s10853-020-04517-6>.